Monitoring Line-Infrastructure With Multisensor SAR Interferometry: Products and Performance Assessment Metrics

Ling Chang, Rolf P. B. J. Dollevoet, and Ramon F. Hanssen, *Senior Member, IEEE*

***Abstract*—Satellite radar interferometry (InSAR) is an emerging technique to monitor the stability and health of line-infrastructure assets, such as railways, dams, and pipelines. However, InSAR is an opportunistic approach as the location and occurrence of its measurements (coherent scatterers) cannot be guaranteed, and the quality of the InSAR products is not uniform. This is a problem for operational asset managers, who are used to surveying techniques that provide results with uniform quality at predefined locations. Therefore, advanced integrated products and generic performance assessment metrics are necessary. Here, we propose several new monitoring products and quality metrics for a-priori and a-posteriori performance assessment using multisensor InSAR. These products and metrics are demonstrated on a 125 km railway line-infrastructure asset in the Netherlands.**

***Index Terms*—Line-infrastructure, satellite radar interferometry (InSAR).**

I. Introduction

MONITORING critical civil infrastructure is arguably one of the most societally beneficial applications of satellite-borne InSAR [1]–[3]. Such infrastructure includes dams, dikes, roads, railways, and pipelines, which are all assets characterized by their extended spatial dimension in one direction, while being limited in the other, i.e., line infrastructure. Several studies have shown the potential of this technology, for various sensors, wavelengths, and resolutions [4]–[11].

However, for practical and operational application development, there are several challenges to overcome. One important challenge is the difference between problem-driven versus data-driven applications of InSAR. Professional asset managers generally have a problem-driven approach. They know what type of information they require to ensure the safety and sustainability of their assets, and solicit for engineering firms to provide exactly the required type of data as defined in the terms of reference. As every specific (part of an) asset has its own specifics, the use of InSAR for this purpose is extremely dependent on the local circumstances, such as the asset's orientation relative to the satellites, its position, and its expected deformation magnitude and direction [12], [13]. As such there is a need for a priori performance assessment metrics, which allows asset managers to make a balanced and well-argued decision to start acquiring and using InSAR data.

The data-driven applications of InSAR require a completely different mindset, which is not common in engineering practice. In this approach, one regards the available observations as proxies for the health of infrastructure. The sheer amount of available data, acquired very frequently, with high-precision, and at very low costs, makes it an attractive source of information, even though this is a rather opportunistic approach, and the measurements are not optimally tuned to a specific problem-definition. However, as the standard data products of InSAR or PSI analyses [2], [14], [15] are still very close to the raw radar measurements, it requires a substantial level of radar knowledge to interpret them correctly. Moreover, if more and more datasets become available from different satellite sources and geometries, there is a need to develop advanced integrated products tuned for asset managers.

Here, we propose several new products and quality metrics for (a priori) performance assessment using multisensor InSAR, focused on generic line infrastructure, with specific examples for railway monitoring. As a general characteristic of line infrastructure, we will use the assumption that deformations occur dominantly in the vertical (normal) and transversal direction, while deformations in the longitudinal direction will be negligibly small, cf. [8] and discussion in Section II-A. See Fig. 1(a) for the definition of the coordinate system. Arguably, this assumption may be challenged for specific cases, but the nature and socio-economic importance of these specific assets, as well as the main forces that act upon them, make it worthwhile to develop theory and tools under this assumption.

This paper is organized as follows. In Section II, we discuss geometric concepts, i.e., the line-of-sight (LOS) vector decomposition and the space-time alignment needed when two or more sensors are used, specifically for line-infrastructure. Then, we propose specific quality metrics and geometric sensitivity and performance assessment methods in Section III. Section IV presents a number of new practical products for asset management, with a particular railway example, followed by discussion and conclusions in Section V.

Manuscript received September 25, 2017; revised November 28, 2017 and January 26, 2018; accepted February 3, 2018. Date of publication March 1, 2018; date of current version May 1, 2018. *(Corresponding author: Ling Chang.)*

L. Chang and R. P. B. J. Dollevoet are with the Department of Structural Engineering, Delft University of Technology, Delft 2628 CN, The Netherlands (e-mail: L.Chang@tudelft.nl; R.P.B.J.Dollevoet@tudelft.nl).

R. F. Hanssen is with the Department of Geoscience and Remote Sensing, Delft University of Technology, Delft 2628 CN, The Netherlands (e-mail: R.F.Hanssen@tudelft.nl).

Color versions of one or more of the figures in this paper are available online at http://ieeexplore.ieee.org.

Digital Object Identifier 10.1109/JSTARS.2018.2803074

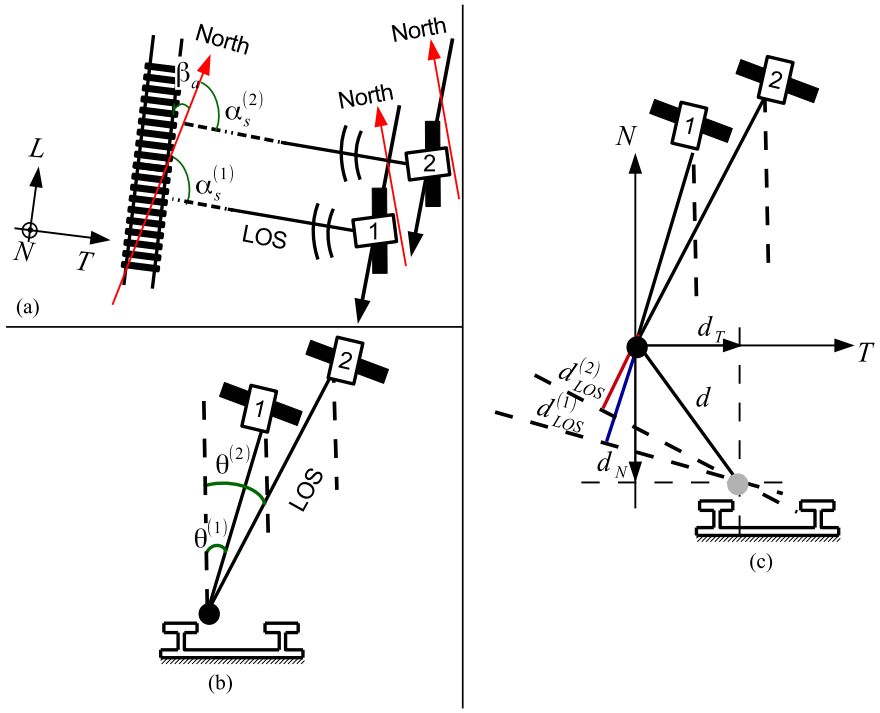

Fig. 1. (a) Top view of two different satellites measuring line-infrastructure (e.g., a railway) in the LOS direction, with azimuth angles $\alpha_s^{(1)}$ and $\alpha_s^{(2)}$ toward satellites 1 and 2, and the local azimuth direction of the asset β_a. The (T, L, N) coordinate system represents the local asset-fixed transversal, longitudinal, and normal axes. (b) Side view. Satellites 1 and 2 observe a ground target indicated by the black dot. The incidence angles are denoted by $\theta^{(1)}$ and $\theta^{(2)}$, respectively. (c) LOS vector decomposition. Due to the target displacement, its position changes from the black to the gray dot. Satellites 1 and 2 measure LOS changes (in red and blue) denoted as $d_{\text{LOS}}^{(1)}$ and $d_{\text{LOS}}^{(2)}$, as a consequence of the transversal movement d_T and normal (≈vertical) movement d_N. Note that the satellite may also observe from opposing headings.

II. Geometric Concepts

A SAR satellite observes line-infrastructure in the form of LOS observations [3]. Here, we first introduce the generic concepts of the LOS vector decomposition to a local, strap-down (asset-fixed) coordinate system, given two (or more) SAR satellite observations. Then, we align all LOS-vector measurements over the asset to common coordinates.

A. LOS-Vector Decomposition

Given displacements in a local, strap-down (asset-fixed), right-handed Cartesian coordinate system, defined as $d_{\text{asset}} = [d_T, d_L, d_N]^T$, see Fig. 1(a), containing three components in transversal, longitudinal, and the complementing normal direction, and centered at the target, the LOS displacement projection is obtained via

$$d_{\text{LOS}} = p^T R_1 R_2 R_3 d_{\text{asset}} \tag{1}$$

where p is the projection vector, with

$$p = [-\sin\theta\cos\alpha_s,\ \sin\theta\sin\alpha_s,\ \cos\theta]^T \tag{2}$$

where α_s is the azimuth angle toward the satellite, corrected for the meridian convergence at the latitude of the asset, and θ is the incidence angle, see Fig. 1(a) and (b). The rotation matrices R_1, R_2, and R_3 are expressed as [16]

$$R_1 = \begin{bmatrix} \cos\beta_a & \sin\beta_a & 0 \\ -\sin\beta_a & \cos\beta_a & 0 \\ 0 & 0 & 1 \end{bmatrix}$$

$$R_2 = \begin{bmatrix} 1 & 0 & 0 \\ 0 & \cos\gamma_s & -\sin\gamma_s \\ 0 & \sin\gamma_s & \cos\gamma_s \end{bmatrix}$$

$$R_3 = \begin{bmatrix} \cos\gamma_t & 0 & \sin\gamma_t \\ 0 & 1 & 0 \\ -\sin\gamma_t & 0 & \cos\gamma_t \end{bmatrix} \tag{3}$$

where β_a represents the azimuth of the longitudinal direction of the asset, relative to the North ($\beta_a \in (-90°, +90°]$), see Fig. 1(a), while γ_s represents the longitudinal slope of the asset (up-hill is positive), and γ_t represents either the cant of the asset (positive for a track curving to the right) or the slope of the side of an embankment. The latter is of importance, e.g., railway applications, see [16].

Obviously, given a single, one-dimensional (1-D), LOS measurement (for a certain target), it is not possible to invert for the three unknown d_{asset} components, cf. (1). As discussed in the introduction, one acceptable constraint is to assume that it is unlikely that there is significant nonelastic deformation in the longitudinal direction [17]. Acknowledging longitudinal strain due to temperature changes in metallic structures, this is

reversible, and will not cause permanent (nonperiodic) localized longitudinal displacements. Moreover, on typical metallic line-infrastructure, such as rails, there are few discrete radar scatterers that will move in longitudinal direction, even though the object itself can extend or contract. Finally, as railways have a maximum slope of 4°, they are by definition always near-orthogonal to the downward direction of land slide motion. Under this assumption, (1) is solvable using at least two LOS measurements from different viewing geometries. For this reason, we assume that this component d_L is equal to zero, which is implemented by using a pseudo-observation $\underline{d}_L$ with low variance, i.e., $\sigma^2_{d,L} = 0.01\ \text{mm}^2$. The mathematic model is then defined as

$$E\left\{\underbrace{\begin{bmatrix}\underline{d}^{(1)}_{\text{LOS}}\\ \underline{d}^{(2)}_{\text{LOS}}\\ \underline{d}_L\end{bmatrix}}_{\underline{d}'}\right\} = \underbrace{\begin{bmatrix}p_{11} & p_{12} & p_{13}\\ p_{21} & p_{22} & p_{23}\\ 0 & 1 & 0\end{bmatrix}}_{A}\underbrace{\begin{bmatrix}d_T\\ d_L\\ d_N\end{bmatrix}}_{d_{\text{asset}}}$$

$$D\left\{\underbrace{\begin{bmatrix}\underline{d}^{(1)}_{\text{LOS}}\\ \underline{d}^{(2)}_{\text{LOS}}\\ \underline{d}_L\end{bmatrix}}_{\underline{d}'}\right\} = \underbrace{\begin{bmatrix}\sigma^2_{d,\text{LOS},1} & 0 & 0\\ 0 & \sigma^2_{d,\text{LOS},2} & 0\\ 0 & 0 & \sigma^2_{d,L}\end{bmatrix}}_{Q_{d'}} \quad (4)$$

where $E\{.\}$ and $D\{.\}$ express the expectation and dispersion operator, respectively. Two LOS-vector measurements with different viewing geometries are denoted by $\underline{d}^{(1)}_{\text{LOS}}$ and $\underline{d}^{(2)}_{\text{LOS}}$, as depicted in Fig. 1(c), and the underline indicates the stochastic nature of the observations. The observation-vector $\underline{d}'$ also contains the pseudo-observation $\underline{d}_L$, which is set to zero if no other information is available. The elements of the projection vector are denoted as p_{ij}, with $i, j \in [1, 2, 3]$. The projection matrix for $\underline{d}^{(1)}_{\text{LOS}}$, $[p_{11}\ p_{12}\ p_{13}]$, is equivalent to $p_1^T R_1 R_2 R_3$, cf. (1), where p_1 is the projection vector for observing $\underline{d}^{(1)}_{\text{LOS}}$, while the projection matrix for $\underline{d}^{(2)}_{\text{LOS}}$, i.e., $[p_{21}\ p_{22}\ p_{23}]$, is derived from $p_2^T R_1 R_2 R_3$, where p_2 is the projection vector for observing $\underline{d}^{(2)}_{\text{LOS}}$. The variances of the two LOS measurements are $\sigma^2_{d,\text{LOS},1}$ and $\sigma^2_{d,\text{LOS},2}$. It is evident that adding more observations, from other satellites or viewing geometries, will increase redundancy in (4) and improve the precision of the estimates. In the unlikely case that (nonperiodic) longitudinal displacements would be significant, the pseudo-observation $\underline{d}_L$ with zero value does not hold in (4) and needs to be replaced by one or more LOS-vector measurements with different viewing geometries w.r.t. $\underline{d}^{(1)}_{\text{LOS}}$ and $\underline{d}^{(2)}_{\text{LOS}}$.

B. Space-Time Alignment

If a specific asset is imaged by SAR from several satellites or from different orbital geometries, the resulting data will consist of disjoint sets of independent time series. For each acquisition geometry, a different set of scatterers will be acquired at different times, i.e., these sets will not be aligned in space and time. This implies that the different subsets can only be used in concert if they are observing the same physical processes. In practice, this means that these physical deformation processes should have some degree of correlation, both in space and time.

Moreover, as the LOS measurements for a certain satellite data stack are all relative to an independent and predefined reference point and reference time, a datum connection is required to bring the stacks in a common datum, see [11] for further discussion on this topic. In practice, unless a dedicated geodetic reference point is available as in [18], the assumed smoothness of the deformation signals in space and time is used to choose a common reference point and relate the data to a common reference time. Note that the noise of the reference point is removed using the *Shenzhen*-algorithm proposed in [19].

III. Quality Metrics and Geometric Sensitivity Analysis

The quality of the LOS-vector decomposition is first discussed by defining the 3-D covariance matrix and the Dilution of Precision (DoP). Then, we discuss the LOS-vector sensitivity and particular observability, and minimal detectable deformation (MDD). We use Envisat and Radarsat-2 as illustration.

A. 3-D Covariance Matrix

Using error propagation for the mathematical model in (4), the precision of the estimated deformation of the asset can be described most completely via the covariance matrix of $\hat{\underline{d}}_{\text{asset}}$, see (1) and (4)

$$Q_{\hat{d}_{\text{asset}}} = (A^T Q^{-1}_{d'} A)^{-1} = \begin{bmatrix}\sigma^2_T & \sigma_{TL} & \sigma_{TN}\\ \sigma_{LT} & \sigma^2_L & \sigma_{LN}\\ \sigma_{NT} & \sigma_{NL} & \sigma^2_N\end{bmatrix} \quad (5)$$

where the subscripts T, L, and N are shorthand notation for the deformations in the asset-fixed coordinate system. The precision is depending mostly on the azimuth of the asset β_a, while it is less affected by changes of the longitudinal slope γ_r and cant γ_t. Moreover, e.g., for railway geometries the longitudinal slope γ_s is less than 4°, and the cant γ_t is less than 6° [17], which implies that R_2 and R_3 are both almost equal to the identity matrix. An example of $Q_{\hat{d}_{\text{asset}}}$ as defined in (5) is visualized in the inset of Fig. 2, for $\beta_a = 45°$. It clearly shows the high precision (low variance) for σ^2_N in the vertical direction, the postulated low variance in the longitudinal direction, and the poorer variance in the transversal direction, as well as the covariances between these parameters.

B. Dilution of Precision

The best description of the expected quality of the estimated parameters is given by the covariance matrix in (5), but it is valuable to present an alternative scalar representation of the quality, i.e., the DoP, which is the purely geometric contribution to the quality of the estimated parameters. Here, we define the DoP for the asset vector $\hat{d}_{\text{asset}}$ as [20]

$$\text{DoP} = (\det(Q_{\hat{d}_{\text{asset}}}))^{\frac{1}{2n}} \quad (6)$$

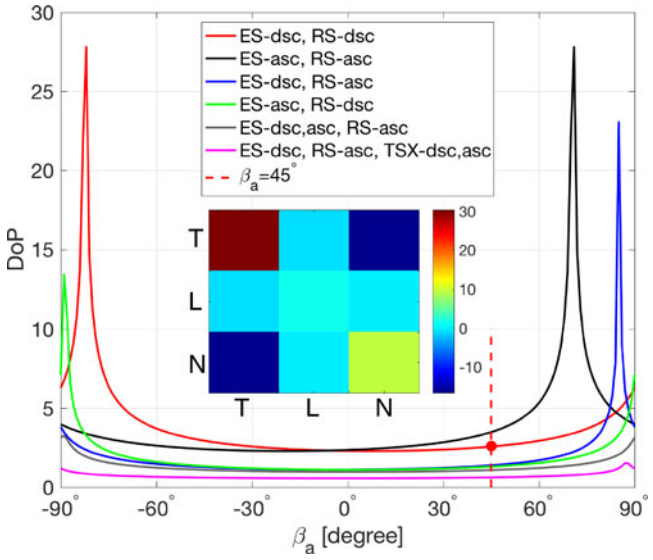

Fig. 2. DoP in relation to varying asset azimuth angles β_a, given different SAR satellite data combinations. The unit of the DoP is equal to the unit of the input observations, i.e., [mm] or [mm/y]. The inset shows the full covariance matrix $Q_{\hat{d}_{\text{asset}}}$, see (5), when $\beta_a = 45°$, given Envisat and Radarsat-2 data in descending orbit, as indicated by the solid red line. The unit of the covariance matrix entries is $[\text{mm}]^2$ or $[\text{mm/y}]^2$. Note that RS-asc, RS-dsc, ES-asc, ES-dsc, and TSX-dsc,asc, represent Radarsat-2 in ascending and descending orbit, Envisat in ascending and descending orbit, and TerraSAR-X in both descending and ascending orbit, respectively.

where $Q_{\hat{d}_{\text{asset}}}$ follows from (5), and det(.) denotes the determinant operator.

The (absolute value) of the determinant represents the volume of a parallellepiped spanned by the three vectors in the covariance matrix $Q_{\hat{d}_{\text{asset}}}$ [21]. As this parallellepiped scales proportional with the error ellipsoid associated with $Q_{\hat{d}_{\text{asset}}}$, a lower DoP represents a smaller solution space, which yields a better anticipated estimation quality. The factor $1/2$ in the exponent is needed to obtain volumetric units, while the factor $1/n$ makes the value of the metric comparable to a standard deviation (SD) of a single (scalar) deformation component. Since there are three components for $\hat{d}_{\text{asset}}$, i.e., d_T, d_L, and d_N, $n = 3$. In case the three components would be uncorrelated with equal variance, resulting in a diagonal $Q_{\hat{d}_{\text{asset}}}$, the DoP would be equal to the SD. The advantage of the formulation in (6) is that in the (more realistic) case of correlated parameters, the single value of the DoP can be used to compare the quality of different solutions. For example, adding another SAR satellite, the resulting quality is improved if the DoP is getting smaller. Fig. 2 illustrates that two satellite datasets that are both acquired from descending (or ascending) orbits, i.e., Envisat and Radarsat-2, yield bigger DoP values, shown in red and black, compared with DoP values (shown in blue and green) for two datasets from opposed orbital directions. When three or more satellites are available, the DoP becomes smaller, shown in gray and purple. Note that the variance values $\sigma^2_{d,\text{LOS}}$ for the LOS estimates are set to 1 for C-band sensors and to 0.25 for X-band sensors, where the unit of these estimates can be $[\text{mm}]^2$ or $[\text{mm/y}]^2$, depending on the observable of interest. The incidence angles and the headings of the TerraSAR-X acquisitions are 23.5° and 192° for descending, 39.2° and 350° for ascending, respectively.

C. Performance Assessment Metrics: Sensitivity Circle

The scalar sensitivity metric $s \in [0, 1]$ is associated to one specific deformation direction, indicated in a 3-D Euclidian space by unit vector $\vec{d}_{\text{asset}}$, given the LOS unit vector $\vec{l}$ from the target to the sensor. It is defined as the inner product of both

$$s = \left| \vec{d}_{\text{asset}} \cdot \vec{l} \right| \tag{7}$$

that is the orthogonal projection of $\vec{d}_{\text{asset}}$ on $\vec{l}$. The metric is useful to assess whether asset deformation in a specific (expected) direction is observable with a specific satellite. For line-infrastructure, assuming orthogonal and normal (vertical) deformations only, we introduce *sensitivity circles*, see Fig 3.

We project the unit deformation vector onto the LOS directions of a number of satellites, with different satellite headings α_s and satellite incidence angles θ, using (4). Considering the possible local azimuth directions of the asset β_a, the *orthogonal elevation angle*, ζ, of the unit deformation vector can vary in the range $(-180°, 180°]$ in a plane orthogonal to the local line-infrastructure azimuth direction, e.g., the rail track direction, see the sketch in the middle of Fig. 3. The angle $\zeta = 0°$ corresponds with a horizontal deformation looking right when facing the asset azimuth (heading) direction of the line-infrastructure, while $\zeta = \pm 180°$ means leftward-looking horizontal deformation. If $\zeta = +90°$, it implies upward vertical deformation. Since the LOS-vector sensitivity values are line-symmetric for a full cycle when $\zeta \in (-180°, 180°]$, we plot the LOS-vector sensitivity circle only in the range $\zeta \in [0°, 180°]$.

Fig. 3 demonstrates the sensitivity circles for one particular location along a line-infrastructure segment, in this case a location along a railway. For example, in Fig. 3(a), the railway track is heading northbound, while in Fig. 3(b), the heading is eastbound. The two colored semi-circles show the sensitivity values, s, for each of the satellites available for this particular asset. A sensitivity of $s = 1$ implies that the geometric quality for that particular deformation vector direction is optimal, while zero sensitivity relates to a deformation vector that is in the null-space of that particular satellite. Thus, a deformation in that particular direction will not be detectable. The sensitivity circle for, e.g., Radarsat-2 ascending (the outermost semi-circle in the plots) indicates a sensitivity value of 0.83 for vertical upward (or downward) deformation. Quantitatively this implies that the SD of the LOS deformation estimates, given the asset azimuth β_a, needs to be divided by this sensitivity value, $\sigma_\zeta(\zeta|\beta_a) = \sigma_{d,\text{LOS}}/s(\zeta)$.

The combination of all available satellite datasets (in this case four) allows us to assess whether a particular deformation can be observed and to which precision. Comparing Fig. 3(a) and (b), it can be observed that for an eastbound infrastructure heading, cf. Fig. 3(b), the alignment of the blue areas indicates that a left- or right-lateral deformation will be nearly impossible to detect, as the LOS-sensitivities are all minimal in that direction.

To visualize the sensitivity circles as a function of the infrastructure heading β_a, (the asset azimuth angle), Fig. 4 shows a 3-D *sensitivity tunnel*, which can be conveniently visualized in a 2-D projection [Fig. 4(a)–(d)] for Radarsat-2 in ascending and descending orbit, and Envisat in ascending and descending

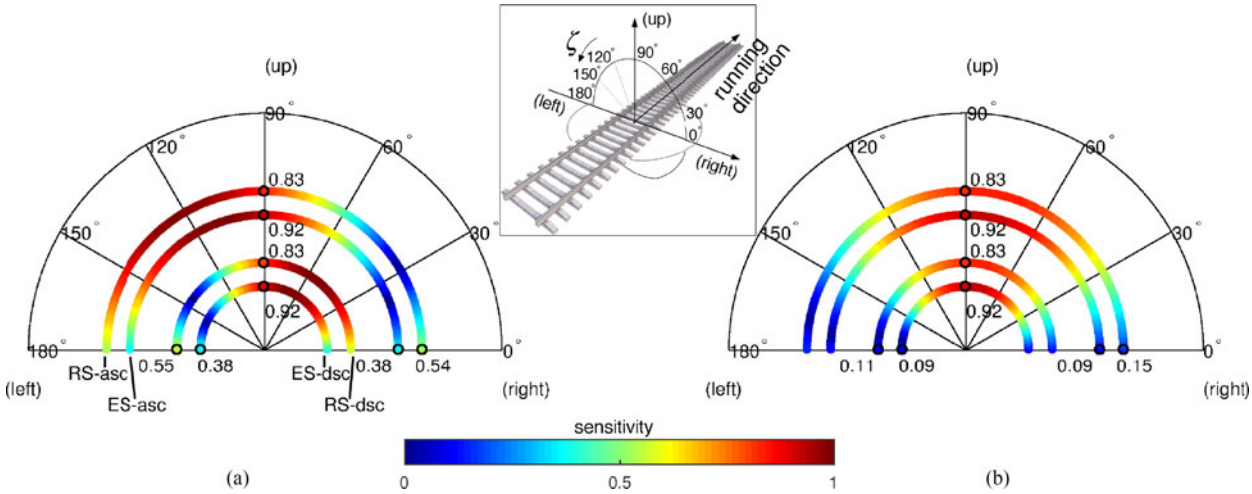

Fig. 3. LOS-vector sensitivity circles for given asset azimuth angle values of line-infrastructure (a) $\beta_a = 0°$, (b) $\beta_a = 90°$. Four rings from outer to inner represent the LOS-vector sensitivity for Radarsat-2 in ascending orbit (RS-asc), Envisat in ascending orbit (ES-asc), Radarsat-2 in descending orbit (RS-dsc), and Envisat in descending orbit (ES-dsc), respectively. The orthogonal elevation angle ζ of the unit deformation vector direction is confined in [0° 180°]. The color represents the scaled sensitivity between [0 1]. The sketch in the middle describes the viewing of the orthogonal elevation angle of the unit deformation vector.

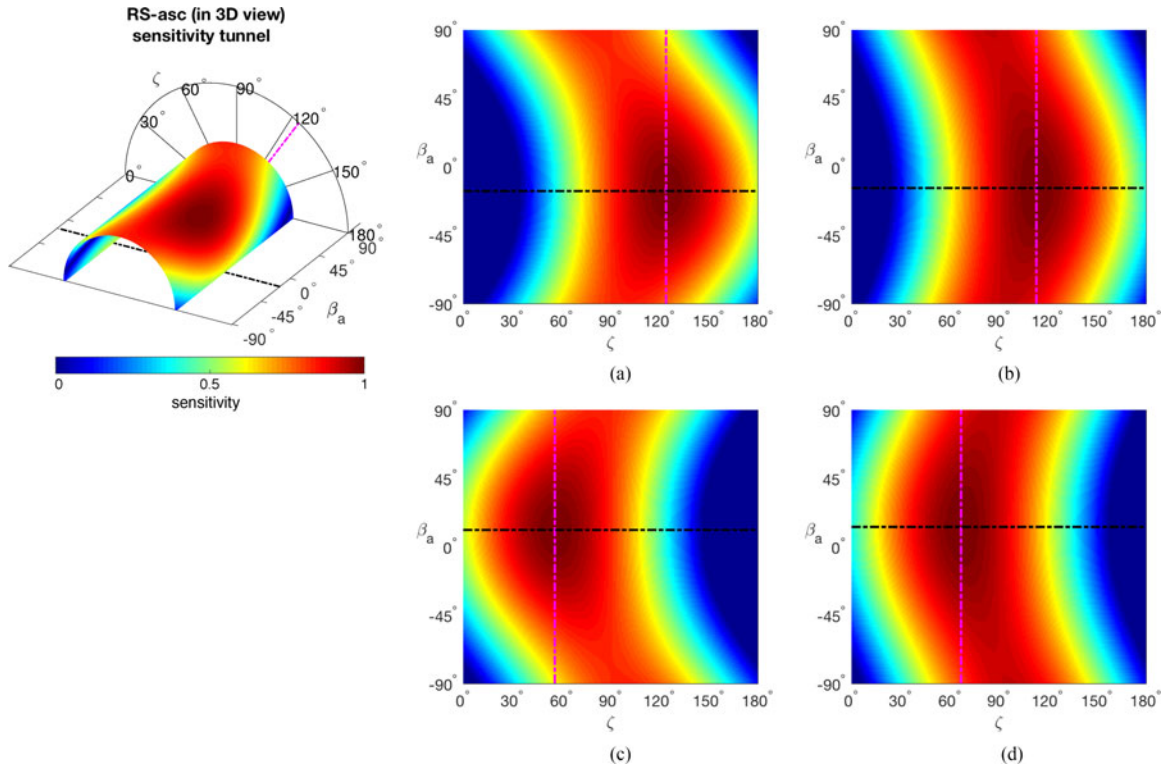

Fig. 4. LOS-vector sensitivity circles visualized for all possible asset azimuth angles β_a, i.e., a *sensitivity tunnel*. (a)–(d) Projection of this sensitivity tunnel in a 2-D plane, for RS-asc, ES-asc, RS-dsc, and ES-dsc, respectively. The asset angle of the line-infrastructure β_a varies in the range $(-90° + 90°]$, the orthogonal elevation angle ζ of the unit deformation vector direction is confined in [0° 180°], and the color represents the LOS-vector sensitivity values between [0 1]. The incidence angles and the satellite heading angles are depicted by the purple and black dashed line, respectively.

orbit. All those four LOS-vector sensitivity circles are projected on the (ζ, β_a)-plane (in 2-D view).

D. Particular Observability

Equation (4) shows the case in which a deformation vector is unknown, both in magnitude as well as direction, and the components of the deformation vector need to be estimated. When an asset manager wants to know whether a deformation, at a given location, p, in a particular direction, ζ, can be detected with InSAR, and with which precision, we can use the sensitivity values for any combination of satellite acquisitions as weights to estimate that deformation. Given a particular set of satellites, and assuming that each satellite yields a representative measurement

at that particular location, the functional and stochastic model can now be expressed as

$$E\left\{\begin{bmatrix} \underline{d}_{p,\mathrm{LOS}}^{(1)} \\ \underline{d}_{p,\mathrm{LOS}}^{(2)} \\ \vdots \\ \underline{d}_{p,\mathrm{LOS}}^{(m)} \end{bmatrix}\right\} = \underbrace{\begin{bmatrix} s_p^{(1)}(\beta_a,\zeta) \\ s_p^{(2)}(\beta_a,\zeta) \\ \vdots \\ s_p^{(m)}(\beta_a,\zeta) \end{bmatrix}}_{\mathbf{A}} x_p(\beta_a,\zeta)$$

$$D\left\{\begin{bmatrix} \underline{d}_{p,\mathrm{LOS}}^{(1)} \\ \underline{d}_{p,\mathrm{LOS}}^{(2)} \\ \vdots \\ \underline{d}_{p,\mathrm{LOS}}^{(m)} \end{bmatrix}\right\} = Q_{d_p,\mathrm{LOS}} \tag{8}$$

where $[\,\underline{d}_{p,\mathrm{LOS}}^{(1)}\ \underline{d}_{p,\mathrm{LOS}}^{(2)}\ \cdots\ \underline{d}_{p,\mathrm{LOS}}^{(m)}\,]^T$ are the measurements in LOS direction from satellites $1,2,\ldots,m$ for a certain point p. There are m $(m \geq 2)$ satellites. Every element $s_p^{(i)}(\beta_a,\zeta)$, $i \in [1,m]$ in the design matrix $\mathbf{A}$ is the LOS-vector sensitivity value for satellite i, $i \in [1,m]$, given the line-infrastructure asset azimuth angle β_a for point p and the orthogonal elevation angle ζ. The unknown $x_p(\beta_a,\zeta)$ is the deformation vector in this particular direction, with $\zeta \in [0°, 180°]$. $Q_{d_p,\mathrm{LOS}}$ is the covariance matrix, in which the LOS variances $\sigma^2_{d_p,\mathrm{LOS},i}$ for each observation i are listed on the diagonal, and there is no correlation between satellites. The variance of the estimator of the unknown parameter vector $\hat{x}_p(\beta_a,\zeta)$ can be derived by

$$\sigma^2_{\hat{x}_p(\beta_a,\zeta)} = (\mathbf{A}^T Q^{-1}_{d_p,\mathrm{LOS}}\mathbf{A})^{-1} \tag{9}$$

where $\mathbf{A}$ is the design matrix of (8).

As an example, given the ascending and descending datasets listed in Table I and Fig. 4, we want to know the precision with which we can estimate a deformation velocity in point p with orthogonal elevation angle ζ. At point p, the asset has an azimuth angle indicated by β_a. The variance of the deformation velocity parameter, $\hat{x}_p(\beta_a,\zeta)$, is depicted in Fig. 5. Here, we assume that the LOS deformation velocities have a SD of $\sigma_{d_p,\mathrm{LOS}} = 1$ mm/y, and that there is no correlation among the four satellite geometries. The asset azimuth angle β_a is in the range $(-90°, 90°]$. A smaller variance increases the "observability" of a particular deformation. Roughly, when $\zeta \in [40°\ 140°]$, the observability for deformation of point p is high when the four satellites are available, as the corresponding variance values are smaller than 1. For example, when $\beta_a = 0°$ or $90°$ and $\zeta = 90°$ (vertical deformation) the Envisat and Radarsat-2 LOS-vector sensitivity values are 0.92, 0.92, 0.83, and 0.83, cf. Fig. 3. Hence, the precision of the unknown parameter $\underline{\hat{x}}_p$ for the values $\beta_a = 0°$ or $90°$, and $\zeta = 90°$ is

$$\begin{aligned}\sigma^2_{\hat{x}_p(\beta_a,\zeta)} &= (\mathbf{A}^T Q^{-1}_{d_p,\mathrm{LOS}}\mathbf{A})^{-1} \\ &\approx 0.33 \cdot \sigma^2_{d_p,\mathrm{LOS}} = 0.33. \end{aligned} \tag{10}$$

Thus, the SD of the estimated deformation velocity in this direction reduces from 1 mm/y to $\sqrt{0.33} = 0.57$ mm/y, cf. Fig. 5. This type of evaluation is valuable for asset managers interested in the observability of a particular deformation, rather than an all-encompassing 3-D covariance analysis.

TABLE I
ENVISAT AND RADARSAT-2 SAR DATA CHARACTERISTICS

Satellite	Envisat		Radarsat-2	
Orbit	ASC	DSC	ASC	DSC
Track	T430	T423	T209	T202
Heading	346°	193°	344°	191°
Incidence angle	23°	23°	34°	34°
Wavelength [mm]	56	56	56	56
Polarization mode	VV	VV	HH	HH
Repeat cycle [days]	35	35	24	24
Start date	/	2006.02.01	/	2010.06.20
End date	/	2010.09.08	/	2016.03.08
Nr. images	/	45	/	78

Note that the ascending data did not cover the entire high-speed railway line (HSL) track, thereby the corresponding Start/End data and the number of images (Nr. images) are not mentioned, as such data is not used for the real case study. Ascending and Descending are written as ASC and DSC, respectively.

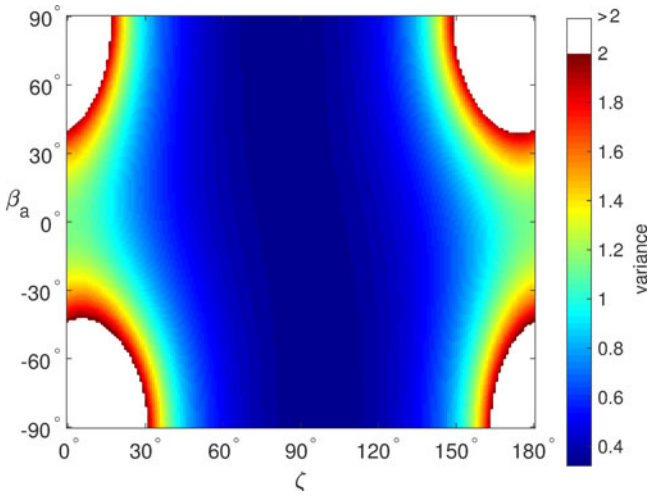

Fig. 5. Variance $\sigma^2_{\hat{x}_p(\beta_a,\zeta)}$ of the unknown parameter $\underline{\hat{x}}_p(\beta_a,\zeta)$, given both Envisat and Radarsat-2 data in ascending and descending orbit. The x-axis represents the orthogonal elevation angles ζ of a unit deformation vector, while the y-axis represents the asset azimuth angles β_a of the line-infrastructure.

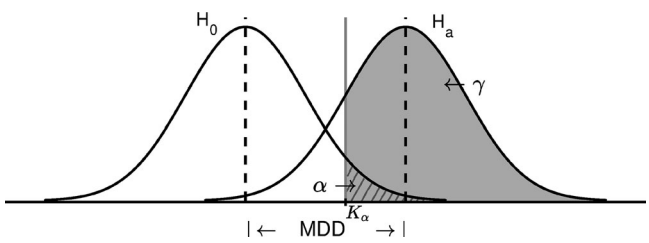

Fig. 6. Probability density functions under the null (no deformation) H_0 and alternative H_a hypothesis. The MDD is the distance between the main modes of both PDFs, and follows from the desired detectability power γ and confidence level $1-\alpha$. The critical value is denoted by K_α.

E. Minimal Detectable Deformation

The SD computed above can be interpreted as a metric for the observability or significance of a deformation signal. By choosing a confidence level $1-\alpha$, where α is the significance level (see Fig. 6), we can compute a critical value K_α [22]. A deformation signal higher than this critical value is considered to be significantly different from the null-hypothesis H_0 that there is no deformation. In other words, we can assess whether

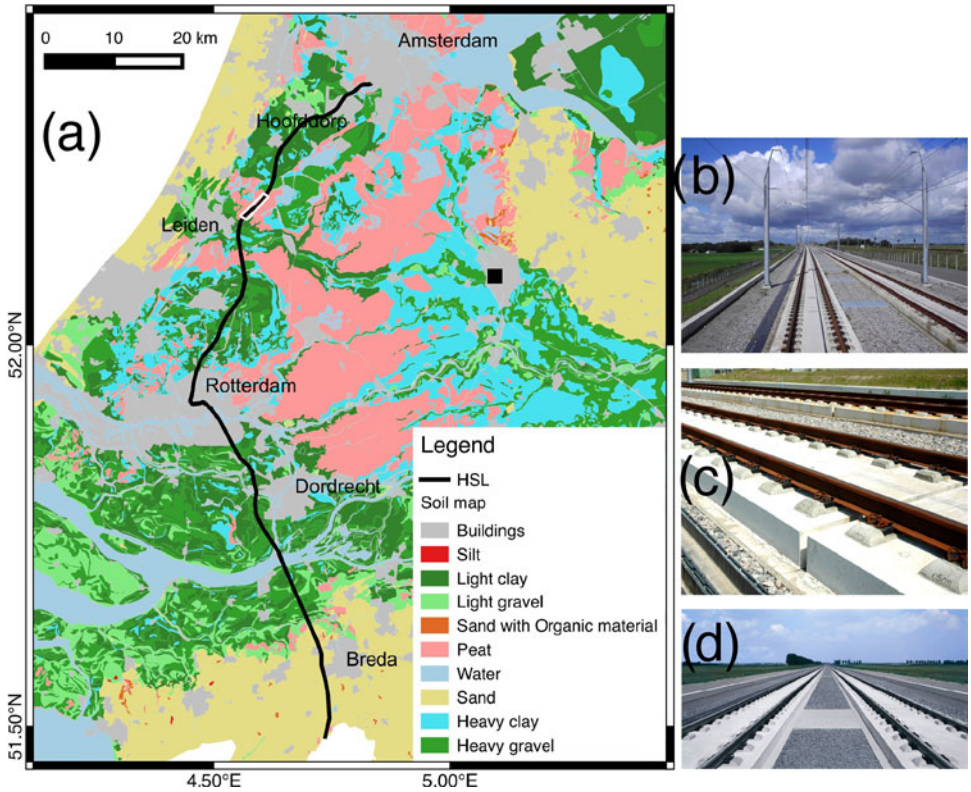

Fig. 7. (a) HSL over a soil map (1:50000, 2006). The HSL is indicated in black, and a specific railway segment over peat soils is indicated by the white rectangle. (b)–(d) Images of the slab track for the HSL (Wiki).

the estimated deformation signal can be explained by noise only, or whether that null-hypothesis needs to be rejected. In Section IV-A, examples for such significant deformation maps (SDMs) are given.

However, from an asset management perspective, one could ask how large a specific deformation should be, to be detectable with a predefined detectability power γ. We refer to this parameter as the MDD. Here, γ is the likelihood that the null-hypothesis of no-deformation is correctly rejected [22], see Fig. 6. Likewise, one could ask with which likelihood (detectability power γ) we can detect a deformation of a predefined value.

With these metrics, asset managers can decide a priori on.

1) The desired confidence level $(1-\alpha)$. Choosing a higher confidence level implies that a particular deformation signal needs to be greater to be recognized as a relevant signal. Consequently, small deformation signals will be missed and not flagged. Choosing a lower confidence level implies that more often false warnings will be issued. In the end, the decision on the confidence level can therefore only be taken by the asset manager, who can weigh the cost of false warnings against the benefits of the correct detection of deformation signals.
2) The desired detectability power γ with which a particular deformation signal should be detectable. Opting for a greater detectability power implies that the MDD becomes greater as well, hence more unfavorable, cf. [19]. The MDD required by asset managers is therefore a metric that can be used to steer the required combination of satellites and resolutions, and consequently assess the potential of InSAR for a particular problem.
3) The desired MDD. Defining this MDD a priori, for example, the maximum strain that a structure can accommodate before failing, allows for the computation of the detectability power γ, given a predefined confidence level $(1-\alpha)$. The γ that follows from this computation will then determine the likelihood that a deformation of this magnitude will be detected.

IV. Practical Products for Asset Management

Operational asset management requires different types of products than those used in the framework of exploratory data analysis, as conventionally used in the InSAR community. In particular, there is a need for products that assist in decision making, and lead to a particular follow-up action. We use a particular use-case to propose some new products, i.e., a 125 km segment of the Dutch high-speed railway between Schiphol airport and Antwerp, HSL, built between 2000 and 2006, and designed to withstand typical soft-soil conditions [17], [23]. In Fig. 7(a), indicated in black, the HSL passes over different soil-types, particularly clay and sand. Some railway segments over peat soils, as, e.g., in the white rectangle, may be strongly affected by ground compaction and groundwater variation. For these areas, a so-called *slab track* was installed where the sleepers are cast into concrete, see Fig. 7(b)–(d). Such concrete and

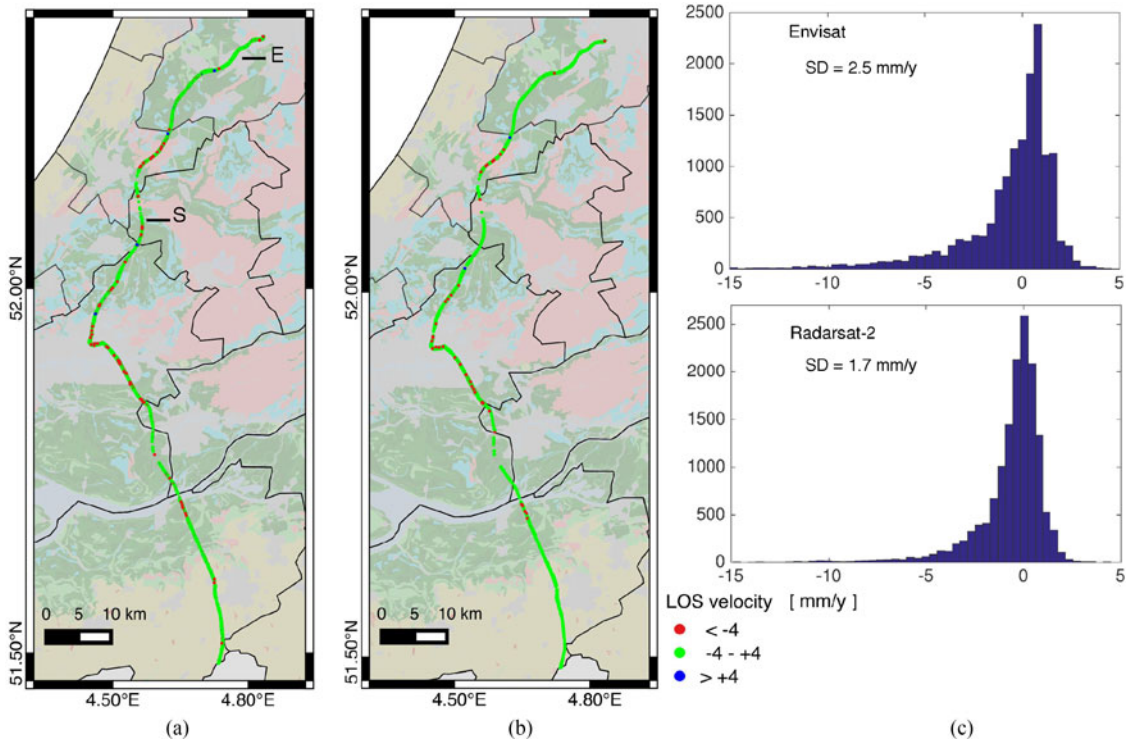

Fig. 8. SDMs of PS points superimposed on a masked soilmap. (a) Envisat. (b) Radarsat-2. (c) Histograms of the LOS deformation velocities of the PS points, to estimate the quality of the deformations as well as the bias between the two independent sets. There are 14667 and 14579 PS points for Envisat and Radarsat-2, respectively. The *x*- and *y*-axes indicate the LOS velocity values and the number of PS points. The SD values of the LOS deformation velocity for Envisat and Radarsat-2 are 2.5 and 1.7 mm/y, respectively.

steel structures exhibit strong backscatter reflectivity characteristics.

We use satellite data acquired after 2006, when the construction of the HSL was finished, from Envisat (45 images acquired between 2006.02 and 2010.09, in VV polarization mode) and Radarsat-2 (78 images acquired between 2010.06 and 2016.03, in HH polarization mode), see Table I. Both datasets were acquired from a descending track (with 11° difference in incidence angle) and cover the entire railway line. Although the two descending tracks may not be perfect in terms of imaging geometry, our aim is to deal with the practical reality for asset managers, where one simply needs to work with the data sources at hand. We want to introduce performance assessment metrics and new asset management products for an arbitrary (nonoptimal) dataset, in order to aid future decisions on the implementation of InSAR for asset management.

In the following, we present maps showing *significant deformation*, as well as itudinal anomaly profiles (LAPs) in Section IV-A. These two products can be produced once LOS deformation time series of satellite measurement points are available. Three other products, introduced in Sections II and III, are discussed in Section IV-B and IV-C: the *decomposition product*, the *DOP*, and the *particular observability*.

A. SDMs and LAPs

Some postprocessing is required to create comparable products of these two datasets. First, to align the Envisat and Radarsat-2 data into a common reference system, see Section II-B, a common reference area (100 × 100 m) is used during the processing, which is indicated by the black square in Fig. 7(a). A 25-m-wide buffer is assigned along HSL and SAR measurements extracted from within that buffer. There are 14667 and 14579 PS points within this buffer for Envisat and Radarsat-2, respectively.

We apply a linear steady-state deformation model for both data sets, extended by a sinusoidal function with a one-year period to account for seasonal effects, see [19]. Fig. 8(a) and (b) shows the SDMs of PS points derived from Envisat and Radarsat-2 SAR images separately. Here, instead of reporting conventional velocities on a continuous scale, as conventionally produced by the InSAR community, we opt for an aggregated product, where we show significant deformations only, with a confidence level of 95%. To achieve this, we need to estimate the noise level of the velocity estimates. We use the histograms of the continuous LOS deformation velocities of the PS points for both satellites, as shown in Fig. 8(c). The histograms show both high deformation velocities, particularly in the extreme left tail of the histograms, as well as the noise level of the estimated velocities. Assuming that it is more likely that railway targets move "away" from the satellite—i.e., downwards—the right tail of the histograms is expected to represent the noise level of the data, as well as unmodeled deformation signal. By fitting a Gaussian probability density function to the histograms, we obtain a (very conservative) empirical estimate of the sum of the noise level and the unmodeled signal. The SDs $\sigma_{\hat{v},\mathrm{LOS}}$ for the

deformation velocities are in the order of 2.0 mm/y. Defining a confidence level 95%, PS points with deformation velocities in the $(-2\sigma, 2\sigma]$ range are labeled green representing "no significant deformation," as shown in Fig. 8(a) and (b). The majority of points (90% for Envisat and 96% for Radarsat-2) does not show significant motion, ≤ 4 mm/y.

Fig. 8(c) also shows that the dispersion of the LOS deformation velocities of the Envisat data (2006–2010) is slightly larger than the Radarsat-2 data (2010–2016), which implies that the temporal behavior of the PS points just after the completion of the HSL construction was more unstable than after 4 years, when the Radarsat-2 data started. The thresholds for the PS point quality, temporal coherence, and minimum/maximum linear deformation velocities are set to be same for both datasets. Regarding the potential driving mechanisms of the deformation, two comments can be made. First, during the years of 2006 and 2009, the rail tracks were not in service, thereby the most-likely driving mechanism for the railway infrastructure instability (i.e., settlement) is soil compaction and rail structure and foundation consolidation that are varying between different types of soils. Second, after 2009, when the railway became operational, the infrastructure was additionally affected by the axle loads of the trains.

With the LOS deformation information for all the PS points, we produce a LAP of the PS point behavior over the HSL railway, see Fig. 9, for an 18 km segment between markers S and E indicated in Fig. 8(a). Fig. 9(a) shows results per hectometer section. If no significant LOS deformation was detected between 2006 and 2010, this is indicated with a small horizontal green line. For all sections where significant deformation is detected, per hectometer interval, this is indicated with a red bar. The height of the red bars indicates how many significantly deforming measurement points are detected in the hectometer section. To discriminate significant and nonsignificant deformation, a 2σ threshold is used, for the Envisat and Radarsat-2 data over this segment, corresponding with a confidence level of 95%. Fig. 9(b) shows the LAP of the PS points for Radarsat-2 between 2010 and 2016. Over some sections, significant deformation is observed by both Envisat and Radarsat-2, which implies that such sections have been unstable over the past ten years. These LAPs can be regularly updated and serve as an instant overview for asset managers.

B. Transversal-Normal Decomposition: Results and Quality

To investigate the transversal and normal (or vertical) deformation components in a local asset-fixed coordinate system, we apply the LOS-vector decomposition method presented in Section II-A, and the estimator quality assessment method from Section III-A, cf. (5).

Fig. 10 shows the LOS deformation velocity map of the $\sim$2.5 km HSL segment over the Rijpwetering area, indicated by the white rectangle in Fig. 7 and by the segment A–A' in Fig. 9. There are 110 and 120 PS points for Envisat and Radarsat-2, respectively, selected over this railway segment. In the subsegment B–B' over a fixed structure, i.e., a bridge, the temporal behavior of the PS points over the evaluated ten years is rela-

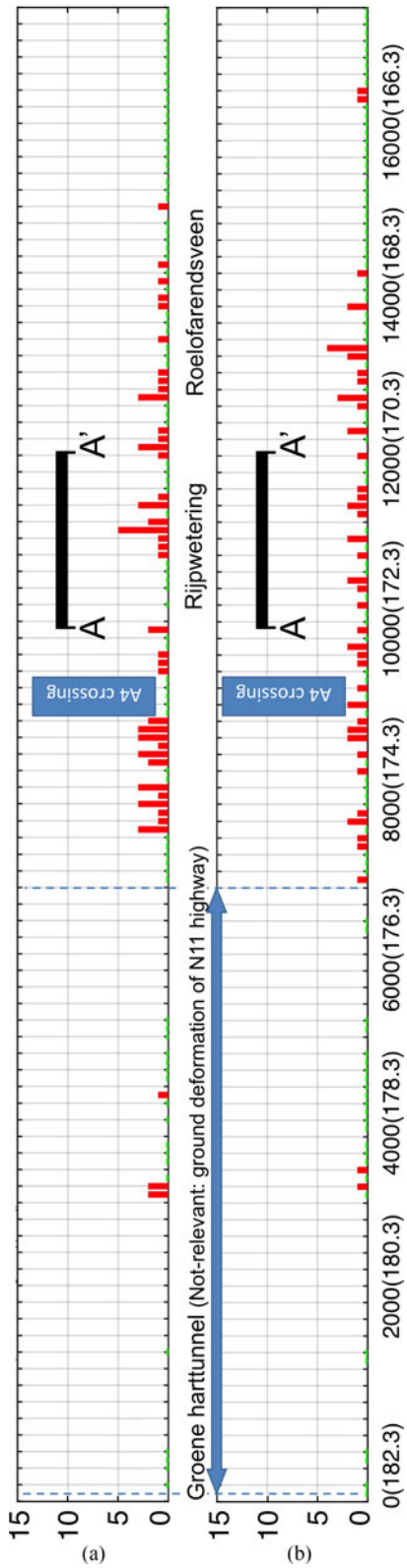

Fig. 9. LAPs of the PS point behavior (deformation velocity [mm/y]) over the 18 km railway segment between $S - E$ (indicated in Fig. 8(a)), during the years of (a) 2006–2010 and (b) 2010–2016. All sections where no significant LOS deformation is detected are indicated with a small green line. For all sections where significant deformation is detected, this is indicated with a red bar. The height of the red bars indicates how many significantly deforming measurement points are detected in that section. The hectometer index numbers are indicated in the brackets.

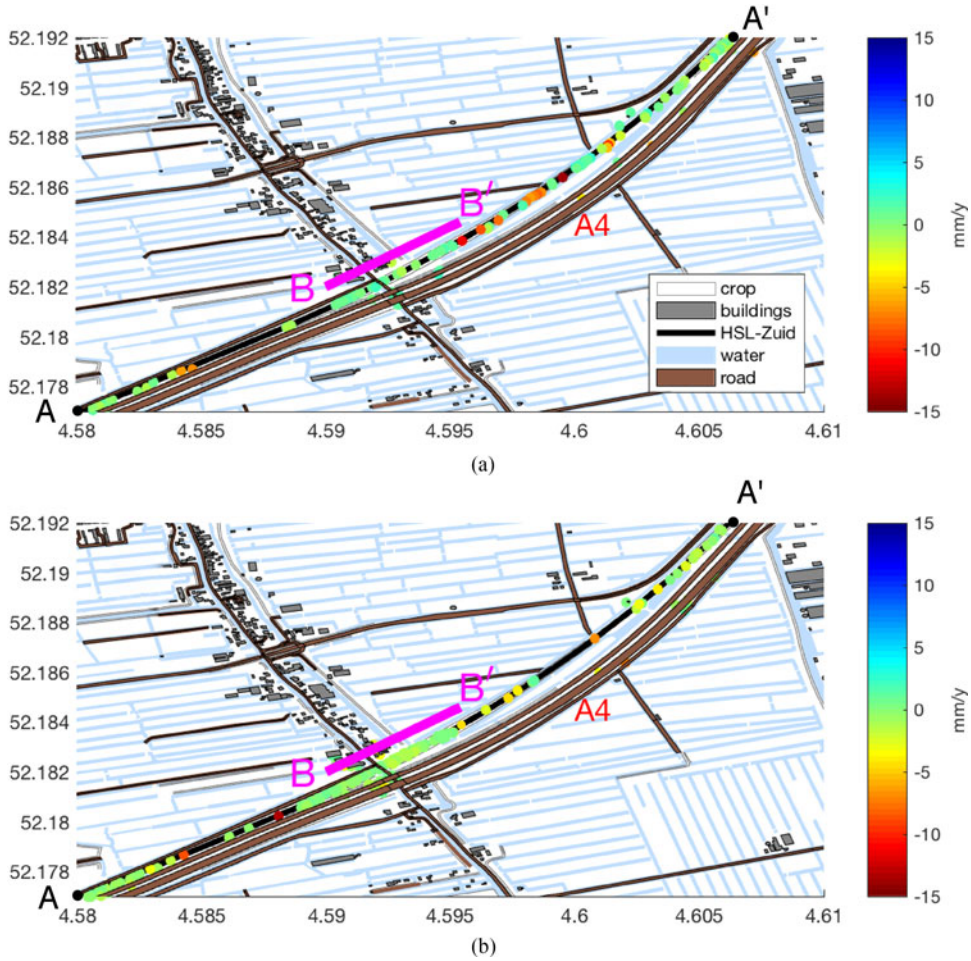

Fig. 10. LOS deformation velocity map of the PS points for (a) 2006–2010 (Envisat, 110 points) and (b) 2010–2016 (Radarsat-2, 120 points) over a ∼2.5 km HSL railway segment at Rijpwetering, indicated by the white rectangle in Fig. 7 as well indicated in Fig. 9.

tively stable, while at the transition zone close to spot B' some PS points are deforming considerably. Because the railway track over a bridge (B–B') has a better structural foundation than a free ballast bed (at B'), it will be less affected by axle loads and ground compaction, showing near-stable temporal behavior. On the other hand, in the *transition zone* between a fixed structure and the free ballast bed, local deformation gradients are expected to occur due to the abrupt stiffness change of the track support.

For operational asset management, the analysis of these two datasets can be based on two different assumptions. First, one could assume that the deformation signal is stationary over time. In that case, the difference in observed deformation velocities between Envisat and Radarsat-2 can be used to decompose the LOS observations into the normal and transversal direction. Alternatively, one could assume that the deformation signal is not stationary over time. In that case, as the two datasets cover two consecutive time ranges, they cannot be used for a vector decomposition any more. Here, we will elaborate on both options.

Following the first hypothesis of temporal stationarity, we first identify corresponding scatterers from both datasets that have a high likelihood of representing the same object. For this, we choose point pairs (tie-points) which have a 3-D distance of less than 1 m, known that the 3-D positioning precision for Envisat and Radarsat-2 measurement points is in the decimeter level, cf. [24]–[26]. We collected 56 point pairs for the LOS-vector decomposition over the Rijpwetering railway segment using (4). The 3-D covariance matrix $Q_{d'}$, see (5), for the point pairs is initialized assuming the SD of LOS displacement per epoch is 5 mm, which yields a formal SD of the LOS velocity of 0.6 and 0.4 mm/y, for Envisat and Radarsat-2, respectively. $Q_{d'}$ is then

$$Q_{d'} = \text{diag}(0.6^2,\, 0.4^2,\, 0.01^2) \tag{11}$$

where the variance in longitudinal direction is postulated to be 0.01^2, while the covariances are set to zero as there is no correlation between those three directions.

The results, see Fig. 11, show that the SD in the transversal direction is two times larger than the SD in the vertical direction, indicated by the gray areas in Fig. 11. This matches the LOS-vector sensitivity discussed in Section III-A. Fig. 11(a) shows the deformation velocities of the 56 point-pairs in the transversal direction over the railway segment A–A', indicated by the black squares. These velocity estimators are rather large and fluctuating, in the transversal direction. The estimator reliability in the

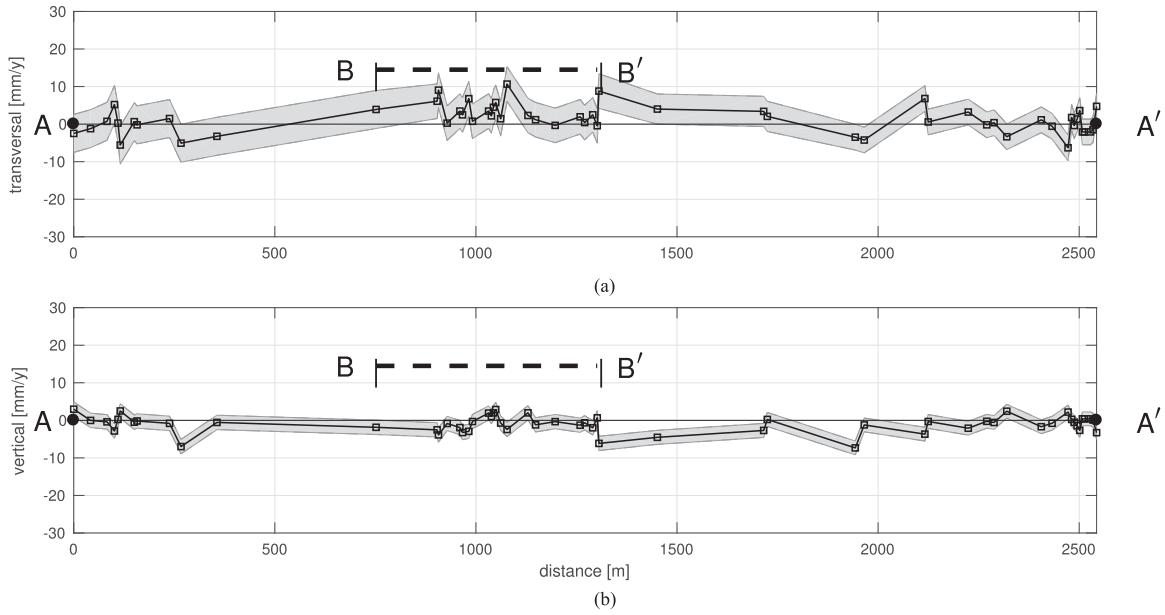

Fig. 11. LOS-vector decomposition results for the Rijpwetering railway segment A–A' as shown in Fig. 10. (a) Deformation velocity in the transversal direction. The positive sign indicates a movement towards the East. (b) Deformation velocity in the vertical direction. The black squares represent the velocity estimators (a) $\hat{d}_T$ and (b) $\hat{d}_N$ for the point-pairs, with the uncertainty shown in gray.

transversal direction is poor for this railway segment, because of the inherent deformation-detection insensitivity of a SAR satellite in West–East direction, cf. Fig. 3(b). Fig. 11(b) shows the deformation velocities of the point-pairs in the vertical direction. In the railway segment over the bridge B–B' with a length of about 500 m, the vertical movements of all the point-pairs are relatively small, while the lateral deformations are greater (eastwards), albeit with a larger uncertainty, see Fig. 11(a), possibly due to the centrifugal forces over this curved and canted railway segment. Note that this potential driving mechanism is hypothesized based on the similar temporal behavior of a cluster of adjacent point-pairs, i.e., all the point-pairs, 22 in total, over the bridge B–B'. In this case, the misinterpretation due to the irregular temporal behavior of any isolated point-pairs can be mitigated. According to *in situ* measurements performed in 2016, the railway segment (the rails in particular) over the bridge B–B' is near-stable in vertical direction and horizontally moving $\sim$15 mm eastward [27].

The alternative hypothesis for interpreting the data of Fig. 10 does not assume temporal stationarity. As both datasets cover different time periods (2006–2010 and 2010–2016), and the HSL railway construction finished only in 2006, it is likely that typical geotechnical consolidation processes exhibit decreasing deformation rates over time. In that case, the LOS deformation rates observed in the 2006–2010 period, e.g., east of point B' in Fig. 10(a), appear to be typically twice as high as those for the 2010–2016 period. The fact that these observations are situated at the same location supports this hypothesis.

The ambiguity in the interpretation of the data segment shown in Fig. 10 demonstrates that the interpretation of PS InSAR data should be performed with the utmost care. In practical situations, datasets are hardly ever ideal, and it is important to understand the different ways in which data can be interpreted. In some cases, an unambiguous conclusion is not possible, and more or other sources of data are needed.

C. DoP and Practical Observability Results

Not all LOS deformations over the HSL railway can be observed by Envisat or Radarsat-2, and the achievable deformation precision varies. One of the reasons is that the LOS deformation precision and sensitivity are varying w.r.t. the rail azimuth angle β_a, the satellite heading α_s and the orthogonal elevation angle ζ, as discussed in Section III. For the Envisat and Radarsat-2 descending datasets, the DoP values and the variance of the deformation velocity estimator are computed based on (5), (6), and (9), and shown in Fig. 12(b) and (c), assuming the variance for the LOS deformation velocity is 0.6^2 (mm/y)^2 for Envisat, and 0.4^2 (mm/y)^2 for Radarsat-2, respectively. Fig. 12(a) shows the rail azimuth angles along the HSL railway. The black line represents the HSL railway, while the colored dots indicate the rail azimuth angle values per rail segment. Here, the rail segment lengths are not uniform. Indicative hectometer index numbers are given at the arrows. Fig. 12(b) shows the DoP values along the HSL railway. The east–west heading railway segments have the highest DoP value, which means the overall integrated quality of the estimated parameters is poor when β_a approaches $\pm 90^\circ$. Contrarily, the overall quality of the estimated parameters is highest for the north–south heading railway segments with a zero β_a.

It is important to note that a high DoP means that the solution space is large. It does not mean that a deformation in a particular direction is less well observable.

The variance of the deformation velocity for all orthogonal elevation angles ζ is shown in Fig. 12(c), in which the color depicts the variance values w.r.t. a varying ζ ($\zeta \in [0^\circ\ 180^\circ]$), given the actual β_a for each rail segment and Envisat and Radarsat-2 satel-

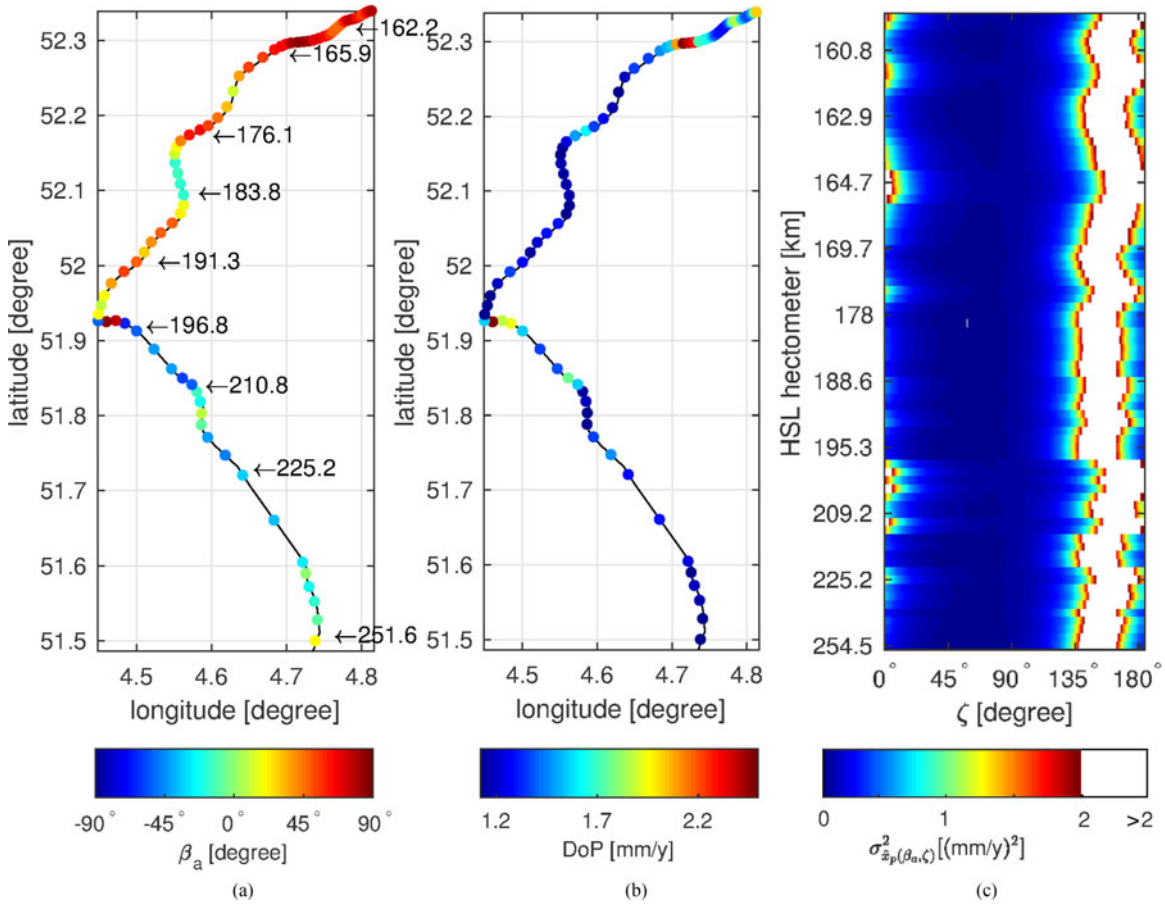

Fig. 12. (a) Rail azimuth angles β_a along the HSL railway. The HSL railway is indicated by black, while the color dots represent the rail heading values over certain rail segments. Some hectometer index numbers are indicated by the arrows. (b) DoP values along the HSL. (c) Variance of the deformation velocity parameter $\underline{\hat{x}}_p(\beta_a, \zeta)$ along the HSL, as a varying ζ ranging in $[0°, 180°]$, given Envisat and Radarsat-2 data in descending orbit.

lite parameters. Although the values vary as per location, when the actual deformation direction ζ is between $\sim [30° 130°]$, the variance value of the deformation velocity in its actual deformation direction is relatively small, which implies that its actual deformation is observable by this combination of satellites, as its SD is less than $\sqrt{0.5}$ (mm/y). When $\zeta >\sim 135°$ or $\zeta <\sim 30°$, the corresponding variance value is considerable, which means that the deformations in those directions are poorly observable with these particular satellites, unless the actual deformation will be very large.

V. Discussion and Conclusion

Operational monitoring of line-infrastructure benefits from the synergistic application of InSAR using multiple satellite missions. Different orbital and instrument viewing geometries, as well as spatial and temporal coverage and resolution, optimize the amount of information that can be extracted from the data. Yet, the applicability and quality of InSAR for this specific type of infrastructure is not guaranteed, nonuniform, and depends on site-specific characteristics. As such, there is a need for dedicated tools and metrics that asset-managers can use to assess this applicability, preferably even before satellite data are acquired. The methods and metrics presented here aspire to achieve this goal, based on the assumptions that:

1) coherent scatterers can be found representing the same relevant phenomenon,
2) alignment of the datasets in space and time is possible, and
3) the influence of (nonperiodic) longitudinal movements compared to transversal and normal motion is limited.

The methods and metrics address two main operational questions.

1) Can we measure a particular deformation in a specific direction, at a specific location, and how well can we measure that?

Sensitivity values and *Sensitivity circles* are introduced, leading to a *deformation variance* as a function of the infrastructure orientation and the *orthogonal elevation angle*. The *particular observability* yields MDDs that can be observed with a given confidence level.

2) What can a particular combination of sensors produce as deformation products, and how does this compare with another combination of sensors?

We state the *method for LOS decomposition* specifically to an asset-based coordinate system, and provide the *variance-covariance matrix* in this coordinate system. The *DoP* is introduced as a scalar-valued quality metric, which is convenient to compare different sensor combinations.

Once InSAR data have been processed into deformation estimates, we introduce two operationally relevant end-products. First, the SDM shows all locations on the selected asset where deformation is significant, given a confidence level as agreed with the asset-manager. Second, the LAPs are a convenient way for instant information on the occurrence, location, and significance of anomalies along the track.

The proposed methods and metrics contribute to a more structured, repeatable, and generic approach in the operational monitoring of line infrastructure.

ACKNOWLEDGMENT

The authors would like to thank the European Space Agency for providing the archived Envisat data and the Netherlands Space Office for routinely acquiring the Radarsat-2 data. Infraspeed is acknowledged for valuable input and feedback.

REFERENCES

[1] R. Bamler and P. Hartl, "Synthetic aperture radar interferometry," *Inverse Problems*, vol. 14, no. 4, pp. R1–54, 1998.

[2] A. Ferretti, C. Prati, and F. Rocca, "Nonlinear subsidence rate estimation using permanent scatterers in differential SAR interferometry," *IEEE Trans. Geosci. Remote Sensing*, vol. 38, no. 5, pp. 2202–2212, Sep. 2000.

[3] R. F. Hanssen, *Radar Interferometry: Data Interpretation and Error Analysis*. Dordrecht, The Netherlands: Kluwer, 2001.

[4] D. Perissin and T. Wang, "Time-series InSAR applications over urban areas in China," *IEEE J. Sel. Topics Appl. Earth Observ. Remote Sens.*, vol. 4, no. 1, pp. 92–100, Mar. 2011.

[5] G. Liu *et al.*, "Exploration of subsidence estimation by persistent scatterer InSAR on time series of high resolution TerraSAR-X images," *IEEE J. Sel. Topics Appl. Earth Observ. Remote Sens.*, vol. 4, no. 1, pp. 159–170, Mar. 2011.

[6] F. Chen, H. Lin, Z. Li, Q. Chen, and J. Zhou, "Interaction between permafrost and infrastructure along the Qinghai–Tibet Railway detected via jointly analysis of C-and L-band small baseline SAR interferometry," *Remote Sens. Environ.*, vol. 123, pp. 532–540, 2012.

[7] D. Perissin, Z. Wang, and H. Lin, "Shanghai subway tunnels and highways monitoring through Cosmo-SkyMed persistent scatterers," *ISPRS J. Photogramm. Remote Sens.*, vol. 73, pp. 58–67, 2012.

[8] L. Chang, R. Dollevoet, and R. Hanssen, "Railway infrastructure monitoring using satellite radar data," *Int. J. Railway Technol.*, vol. 3, pp. 79–91, 2014.

[9] L. Chang and R. Hanssen, "Detection of permafrost sensitivity of the Qinghai–Tibet Railway using satellite radar interferometry," *Int. J. Remote Sens.*, vol. 36, no. 3, pp. 691–700, 2015.

[10] A. M. Arsénio, P. Dheenathayalan, R. Hanssen, J. Vreeburg, and L. Rietveld, "Pipe failure predictions in drinking water systems using satellite observations," *Struct. Infrastructure Eng.*, vol. 11, no. 8, pp. 1102–1111, 2015.

[11] L. Chang, R. Dollevoet, and R. F. Hanssen, "Nation-wide railway monitoring using satellite SAR interferometry," *IEEE J. Sel. Topics Appl. Earth Observ. Remote Sens.*, vol. 10, no. 2, pp. 596–604, Feb. 2017.

[12] Y. Fialko, M. Simons, and D. Agnew, "The complete 3-D surface displacement field in the epicentral area of the 1999 mw7. 1 hector mine earthquake, California, from space geodetic observations," *Geophys. Res. Lett.*, vol. 28, no. 16, pp. 3063–3066, 2001.

[13] T. J. Wright, B. E. Parsons, and Z. Lu, "Towards mapping surface deformation in three dimensions using InSAR," *Geophys. Res. Lett.*, vol. 31, 2004.

[14] B. Kampes, *Displacement Parameter Estimation Using Permanent Scatterer Interferometry*, (ser. Forschungsbericht). DLR, Bibliotheks- und Informationswesen, Braunschweig, Germany, 2005.

[15] F. J. van Leijen, *Persistent Scatterer Interferometry Based on Geodetic Estimation Theory*. Netherlands Geodetic Commission, Delft, The Netherlands, 2014.

[16] L. Chang, R. Dollevoet, and R. Hanssen, "Railway infrastructure monitoring using satellite radar data," *Int. J. Railway Technol.*, vol. 3, pp. 79–91, 2014.

[17] C. Esveld, *Modern Railway Track*. MRT-Productions, Zaltbommel, The Netherlands, 2001.

[18] P. Mahapatra, H. v. der Marel, F. van Leijen, S. Samiei-Esfahany, R. Klees, and R. Hanssen, "Insar datum connection using GNSS-augmented radar transponders," *J. Geodesy*, Jun. 2017. [Online]. Available: https://doi.org/10.1007/s00190-017-1041-y

[19] L. Chang and R. F. Hanssen, "A probabilistic approach for InSAR time-series postprocessing," *IEEE Trans. Geosci. Remote Sens.*, vol. 54, pp. 421–430, 2015.

[20] P. J. G. Teunissen and D. Odijk, "Ambiguity dilution of precision: Concept and application," in *Proc. ION-97*, Kansas City, MO, USA, September 16–19, 1997, pp. 891–899.

[21] D. Lay, *Linear Algebra and Its Applications*. London, U.K.: Pearson Education, 2002. [Online]. Available: https://books.google.nl/books?id=v8Zls26Y0wkC

[22] W. Baarda, *A Testing Procedure for Use in Geodetic Networks*, (ser. Publications on Geodesy), 2nd ed. Delft, The Netherlands: Netherlands Geodetic Commission, 1968, vol. 5.

[23] R. Woldringh and B. New, "Embankment design for high speed trains on soft soils," in *Proc. 12th Eur. Conf. Soil Mech. Geotech. Eng.*, 1999, vol. 3, pp. 1–10.

[24] D. Small, B. Rosich, A. Schubert, E. Meier, and D. Nüesch, "Geometric validation of low and high-resolution ASAR imagery," in *Proc. Envisat ERS Symp.*, vol. 572, 2005, pp. 1–9.

[25] D. Perissin, "Validation of the submetric accuracy of vertical positioning of PSS in c-band," *IEEE Geosci. Remote Sens. Lett.*, vol. 5, no. 3, pp. 502–506, Jul. 2008.

[26] P. Dheenathayalan, D. Small, A. Schubert, and R. F. Hanssen, "High-precision positioning of radar scatterers," *J. Geodesy*, vol. 90, no. 5, pp. 403–422, 2016.

[27] Infraspeed, Private Communication, 2016.

Ling Chang received the M.S.E. degree in geodesy and survey engineering from Tongji University, Shanghai, China, in 2010, and the Ph.D. degree in geodetic engineering from the Delft University of Technology, Delft, The Netherlands, 2015.

Since 2018, she has been an Assistant Professor of microwave remote sensing with the ITC, University of Twente, Enschede, The Netherlands. Her current research interests include statistical hypothesis testing, time series modelling, and change detection, using satellite-borne remote sensing technology, with a focus on rail and infrastructure monitoring.

Rolf P. B. J. Dollevoet received the M.Sc. degree in mechanical engineering from Eindhoven University of Technology, Eindhoven, The Netherlands, in 2001, and the Ph.D. degree in mechanical engineering from the University of Twente, Enschede, The Netherlands, 2010.

Since 2003, he has been with the ProRail, Utrecht, The Netherlands. Since 2012, he has been a part-time Professor with the Section of Road and Railway Engineering, Delft University of Technology, Delft, The Netherlands. He is also currently the Leader of scientific research on rolling contact fatigue and wheel-rail interface within ProRail Civil Engineering.

Dr. Dollevoet is the Chair of the International Union of Railways working group on wheel-rail conditioning and lubrication.

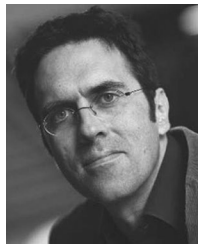

Ramon F. Hanssen (M'04–SM'15) received the M.Sc. degree in geodetic engineering and the Ph.D. (*cum laude*) degree in geodetic engineering from the Delft University of Technology, Delft, The Netherlands, in 1993 and 2001, respectively.

He was with the International Institute for Aerospace Survey and Earth Science, Stuttgart University; the German Aerospace Center (DLR); Stanford University (Fulbright Fellow); and the Scripps Institution of Oceanography where he worked on microwave remote sensing, radar interferometry, signal processing, and geophysical application development. Since 2008, he has been an Antoni van Leeuwenhoek Professor in earth observation with the Delft University of Technology. He is the author of a textbook on radar interferometry.